Low Mach number prediction of the acoustic signature of fractal-generated turbulence

Sylvain Laizet [a,*] Veronique Fortuné [b] Eric Lamballais [b]
John Christos Vassilicos [a]

[a] *Turbulence, Mixing and Flow Control group,*
Department of Aeronautics, Imperial College London,
South Kensington Campus, London SW7 2AZ, UK

[b] *Department of Fluid Flow, Heat Transfer and Combustion, Institute PPRIME,*
Université de Poitiers, ENSMA, CNRS,
Téléport 2 - Bd. Marie et Pierre Curie B.P. 30179
86962 Futuroscope Chasseneuil Cedex, France

Abstract

In this work, we compare the acoustic properties of a fractal square grid with those of a regular grid by means of a hybrid approach based on Lighthill's analogy and Direct Numerical Simulation (DNS). Our results show that the sound levels corresponding to our fractal square grid of three fractal iterations are significantly reduced by comparison to a regular grid of same porosity and mesh-based Reynolds number. We also find a well-defined peak at a Strouhal number between 0.2 and 0.3 in the acoustic spectrum of our fractal square grid which is absent in the case of our regular grid. We explain this effect in terms of a new criterion for quasi-periodic vortex shedding from a regular or fractal grid.

Key words: Direct Numerical Simulation, acoustic predictions,
multiscale-generated turbulence, immersed boundary method, Lighthill analogy.

* Corresponding author.
Email addresses: s.laizet@imperial.ac.uk (Sylvain Laizet),
veronique.fortune@lea.univ-poitiers.fr (Veronique Fortuné),
lamballais@univ-poitiers.fr (Eric Lamballais),
j.c.vassilicos@imperial.ac.uk (John Christos Vassilicos).

1 Introduction

Recent research on turbulence generated by fractal grids [11, 21, 25] showed that such flows have some unusual properties which could be interesting for noise reduction. Experimental measurements [22, 23] undertaken in an anechoic chamber have shown that a reduction in sound pressure levels was obtained at low frequencies, while an increase in sound pressure levels was obtained at high frequencies, and overall, a slight reduction in sound pressure levels was recorded with inclined fractal spoilers relative to inclined solid and regular grid spoilers.

Our aim in the present work is to use DNS for the investigation of the acoustic field generated by a fractal grid and compare with that of a regular grid. A fractal square grid and a regular grid (see figure 1) of equal blockage ratio and mesh-based Reynolds number are investigated and compared in order to capture the influence of the shape of the grid on the acoustic field, but also to attempt to understand how the acoustic field is modified when it is generated at different scales simultaneously.

Identifying the mechanisms responsible for the production of sound by turbulent flows remains to date an extremely difficult task, even for very extensively studied problems, like jet noise. Experimental studies are generally not sufficient when knowledge about the physical mechanisms of noise production is required. DNS allow the calculation of all unsteady flow quantities and can help to investigate the aerodynamically generated sound. The direct computation of sound by solving the compressible Navier-Stokes equations provides both the aerodynamic field and the acoustic field simultaneously [7, 6, 1], but the very high cost of this direct approach remains a limiting factor. As a result, flow-generated acoustic fields are often predicted via a hybrid approach [24, 10], using acoustic analogies or wave extrapolation methods.

In the present work, DNS of turbulent flows generated by a regular and a fractal grid are carried out as in [17], thanks to a novel efficient parallel version of a solver called **Incompact3d** which solves the incompressible Navier-Stokes equations [13, 14, 15]. The acoustic radiation from the flow across the grids is then evaluated thanks to a hybrid approach based on the Lighthill acoustic analogy.

2 Flow simulations

The main goal of the flow simulations reported in this section is to provide the velocity and pressure fields necessary for the evaluation of the acoustic

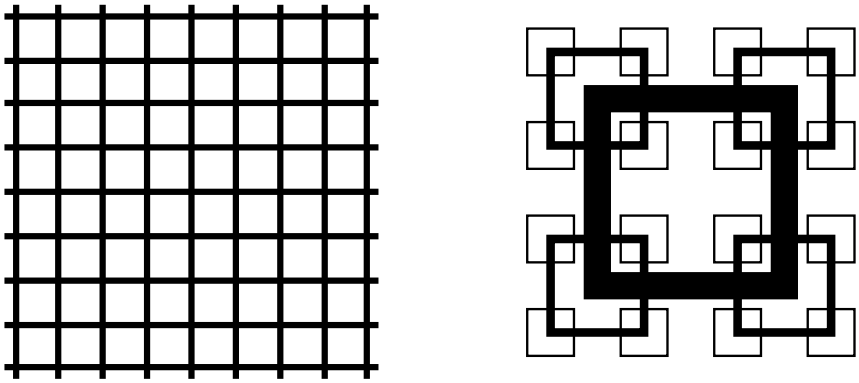

Fig. 1. *Scaled diagrams of the two different grids used in this numerical study: a regular grid (left) and a fractal square grids with an aspect ratio* t_r *of* 8.5 *(right), where* t_r *is the ratio between the biggest and smallest lateral thicknesses.*

sources and associated sound radiation for each grid.

2.1 Numerical methods

To solve the incompressible Navier-Stokes equations, we use the in-house numerical code **Incompact3d** which is based on sixth-order compact schemes for spatial discretization and a third-order Adams-Bashforth scheme for time advancement. To treat the incompressibility condition, a fractional step method requires to solve a Poisson equation. This equation is fully solved in spectral space via the use of relevant 3D Fast Fourier transforms (FFT). With the help of the concept of modified wavenumber introduced by [18], the divergence free condition is ensured up to machine accuracy.

The modelling of the grids is performed by an Immersed Boundary Method (IBM). The present IBM is a direct forcing approach that ensures the no-slip boundary condition at the wall of the grid. The idea is to force the velocity to zero at the wall of the grids, as our particular Cartesian mesh does conform with the geometries of the grids. Note finally that the pressure and velocity mesh are staggered by half a mesh to avoid spurious pressure oscillations introduced by the IBM. More details about the present code and its validation, especially the original treatment of the pressure in spectral space, can be found in [13].

Because of the size of the simulations, the parallel version of **Incompact3d** has been used. Based on a highly scalable new 2D decomposition library and a distributed FFT interface, this code can be used on thousands of computational cores. More details about this efficient parallel strategy can be found in [15].

2.2 Description of the grids

The fractal square grid consists of different sized squares placed in a fractal-square-like pattern (see figure 1, right). The fractal grid is completely characterised by: (i) its number of fractal iterations, here $N = 3$; (ii) its number 4^j of square patterns at iteration j ($j = 0, 1, 2$ for $N = 3$); (iii) its lengths $L_j = R_L^j L_0$ and lateral thicknesses $t_j = R_t^j t_0$ (in the plane of the grid, normal to the mean flow) of the bars making the squares at iteration j. Here, $R_t = 0.343,\ R_L = 1/2,\ L_0 = 0.5L_y$, where L_y and L_z (with $L_y = L_z$) are the lateral sizes of the computational domain (see figure 2); (iv) its thickness ratio $t_r \equiv t_0/t_2 = t_{max}/t_{min} = 8.5$, i.e. the ratio between the lateral thickness of the bars making the largest square and the lateral thickness of the smallest.

The blockage ratio σ of the two grids, defined as the ratio of their total area in the lateral plane to the area $T^2 = L_y \times L_z$, is $\approx 32\%$. The fractal square grid considered here does not have a well-defined mesh size. This is why [11] introduced an effective mesh size for multiscale grids, $M_{eff} = \frac{4T^2}{P}\sqrt{1-\sigma}$ where P is the perimeter length in the $(y-z)$ plane of the zero-thickness fractal grid, i.e. where all thicknesses t_j have been artificially set to zero for the calculation of P. The multiscale nature of the fractal grid influences M_{eff} via the perimeter P which can be extremely long in spite of being constrained to fit within the area $T^2 = L_y \times L_z$. However, this definition of M_{eff} also returns the regular mesh size M, when applied to the regular grid.

The effective mesh size is fully determined by our choices of parameters characterising the fractal grid and it turns out that $M_{eff} = (40/3)t_{min}$. The regular grid considered here has its mesh size M equal to the effective mesh size of the fractal grid. The lateral thickness of the bars t_b making the regular grid is uniquely determined by $\sigma = \frac{t_b}{M}(2 - \frac{t_b}{M})$ and M. In terms of minimum lateral thickness t_{min} of the fractal grid it is $t_b = 2.6t_{min}$. Note finally that the streamwise thickness of the bars for both grids is $2.4t_{min}$.

2.3 Numerical parameters

The computational domain is $L_x \times L_y \times L_z = 460.8t_{min} \times 115.2t_{min} \times 115.2t_{min}$ discretized on a Cartesian mesh of $n_x \times n_y \times n_z = 2305 \times 576 \times 576$ mesh nodes. It is split in 3,456 computational cores. For each grid, the simulation is performed with a Reynolds number $Re_{M_{eff}} = 4000$ (based on M_{eff} and the streamwise upstream velocity U_∞, this Reynolds number value corresponds to a velocity of about $2.5m/s$ in a wind tunnel at usual ambient conditions).

Inflow/outflow boundary conditions are used in the x-direction and periodic boundary conditions in the y direction for $-L_y/2$ and $L_y/2$ and in the z

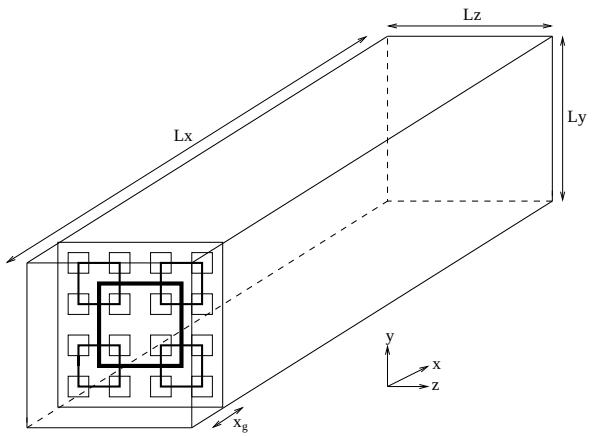

Fig. 2. Schematic view of the flow configuration for the fractal square grid.

direction $-L_z/2$ and $L_z/2$. The time step $\Delta t = 0.015 t_{min}/U_\infty$ is low enough to satisfy the CFL condition. The streamwise position of the grids ($x_g = 10 t_{min}$ from the inflow boundary of the computational domain, see figure 2) has been carefully chosen to avoid any spurious interactions between the modelling of the grid and the inflow boundary condition (see figure 2 for a schematic view of the flow configuration). The inflow profile is a uniform flow field U_∞ without any turbulence perturbations.

2.4 Illustration of the turbulent flows

An illustration of the flow obtained in both cases is given in figure 3, where enstrophy isosurfaces are plotted. These isosurfaces are the enstrophy normalised by its maximum over the $y-z$ plane at the $x-$position considered, and as a result the decay of the turbulence is not visible on these plots. The one obvious difference in these visualizations between the turbulent flow generated by the regular grid and the turbulent flow generated by the fractal square grid is that the latter is clearly more intermittent. The fact is also that these two different types of turbulent flows are generated in different ways. In the regular grid case, same-size wakes interact within a couple of mesh sizes from the grid and mix together in a uniform fashion close to the grid. In the fractal grid case, [16, 21, 17] suggested that the smallest bars on the grid generate the smallest wakes which meet and mix together at the smallest distance from the grid, whereas larger bars generate larger wakes which meet and mix at a further distance from the grid, and that this process repeats itself from the smallest to the largest turbulence-generating scales on the grid in a way which causes the turbulence to progressively intensify over a protracted distance from the grid. The turbulence generation followed by the turbulence decay are clearly visible in figure 4 (left) for both grids. In this figure, we plot the maximum of the turbulent kinetic energy k_{max} over every $(y-z)$ plane as a function

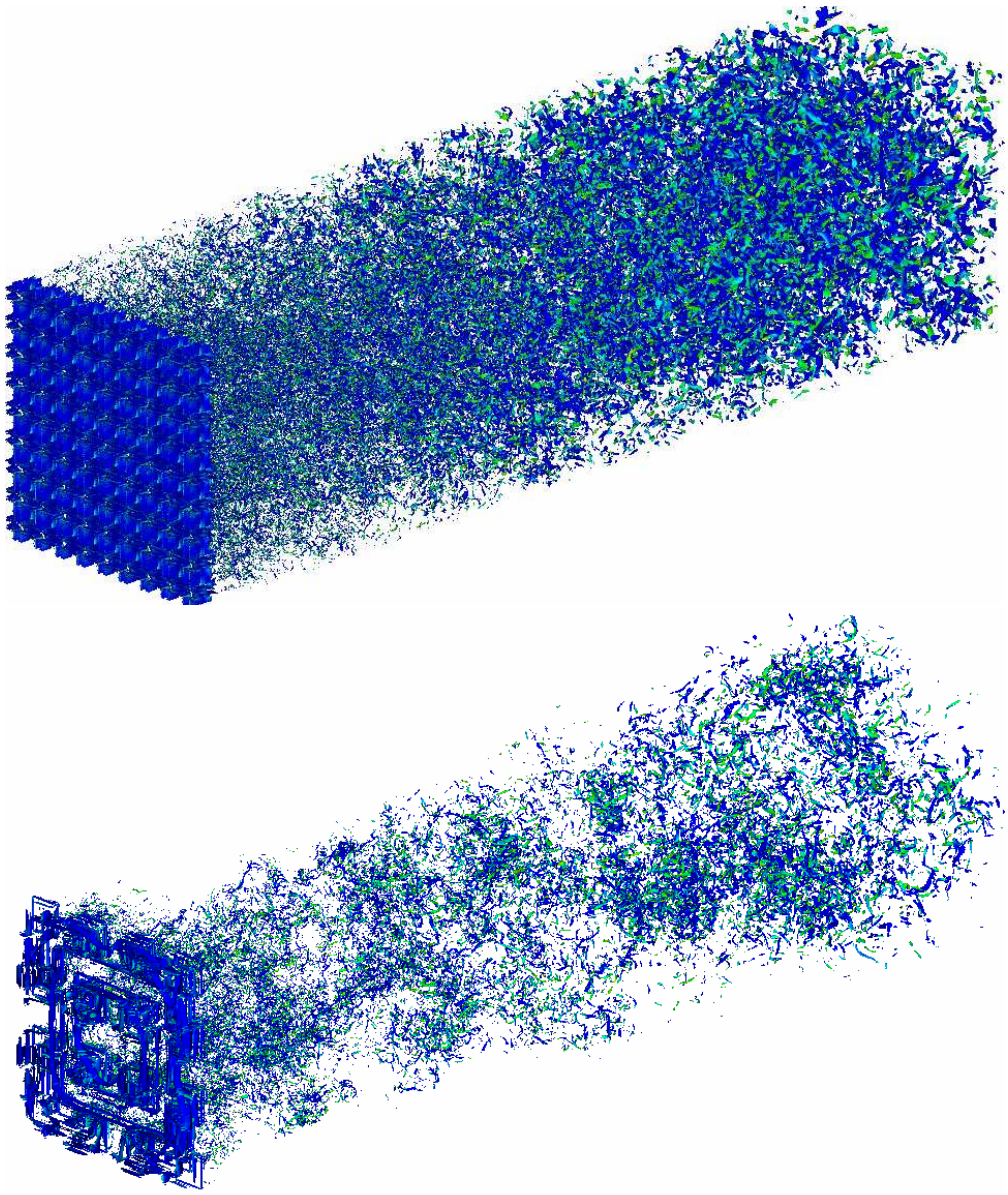

Fig. 3. *Turbulent flows generated by the regular grid (top) and by the fractal grid (bottom). Specifically, 3D isosurfaces of (in blue) the absolute value of the enstrophy vector normalised by its maximum over the* $y-z$ *plane at the x-position considered and of (in green) the* $x-$*component of the vorticity normalised by its maximum over the* $y-z$ *plane at the x-position considered. The value on both isosurfaces is* 0.7.

of the streamwise coordinate x. It is clear from this figure that the present fractal grid generates higher turbulent kinetic energy than the regular grid, even very close to the grid. This trend is confirmed in figure 4 (right) where we plot the streamwise evolution along the centreline of the Reynolds number $Re_\lambda = u'\lambda/\nu$ based on the Taylor micro-scale. Note that the spatial resolution in the present simulation is such that the mesh lengths $\Delta x = \Delta y = \Delta z \leq 4\eta$ in the entire domain, where $\eta = \nu^{3/4}\varepsilon^{-1/4}$ is the Kolmogorov scale, and ε is

the turbulent kinetic energy dissipation rate per unit mass. The fractal square grid generates values of Re_λ about three times larger than the regular grid in the downstream centreline region $200 < x/t_{min} < 450$ for the same $Re_{M_{eff}}$ and the same blockage ratio. The experimental results obtained by [11] with fractal square grids also showed a significant enhancement of Re_λ values over the extent of the downstream decay region which they were able to probe.

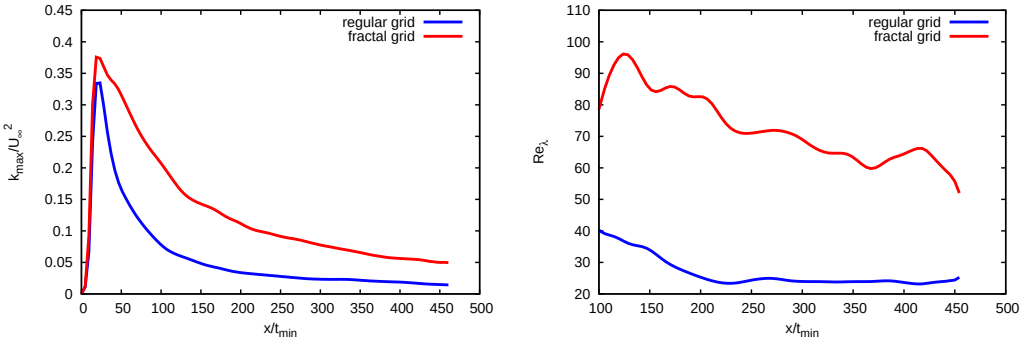

Fig. 4. *Streamwise evolution of the maximum of the turbulent kinetic energy (left) and the Reynolds number based on the Taylor micro-scale (right) along the centreline for the two grids.*

A detailed analysis of the flow dynamics can be found in [17]. The main results of their study are as follows: (i) fractal square grids generate protracted regions of higher vorticity and turbulence intensity than regular grids (except very close to the grid and perhaps also extremely far downstream where the turbulence generated by either grid has decayed so much that the local turbulent Reynolds numbers have become comparably small); (ii) the vorticity field is more intermittent or more clustered when generated by fractal square grids than by regular grids, at least in the downstream region accessed by the simulations; (iii) the flow holds clear geometrical imprints of the turbulence-generating grids quite far downstream, especially for the fractal square grids; (iv) two turbulent regions can be clearly observed, one where the turbulence progressively amplifies closer to the grid followed by one where the turbulence decays.

In the following section, we investigate the sound production associated with the turbulent flow for both grids.

3 Methodology for acoustic prediction

The acoustic fields generated by the flow across each grid are evaluated via a hybrid approach based on the Lighthill analogy [19]. Lighthill's equation is an exact reformulation of the Navier-Stokes equations in order to obtain an inhomogeneous wave equation describing the sound generated in a medium

at rest by the fluctuating stresses embedded in a localised domain, called the source domain. The associated solution can be obtained with the use of a Green function. As in our configuration the source domain also involves solid boundaries, we use the following formulation of the integral solution, following [4] and [5]

$$
\begin{aligned}
p_a(\mathbf{x},t) &= \frac{1}{4\pi}\frac{\partial^2}{\partial x_i \partial x_j}\int\limits_V T_{ij}\left(\mathbf{y}, t-\frac{|\mathbf{x}-\mathbf{y}|}{c_0}\right)\frac{dV}{|\mathbf{x}-\mathbf{y}|} \\
&- \frac{1}{4\pi}\frac{\partial}{\partial t}\int\limits_S \rho u_i\left(\mathbf{y}, t-\frac{|\mathbf{x}-\mathbf{y}|}{c_0}\right) n_i \ \frac{dS}{|\mathbf{x}-\mathbf{y}|} \\
&+ \frac{1}{4\pi}\frac{\partial}{\partial x_i}\int\limits_S \left(\rho u_i u_j + p\delta_{ij} - \tau_{ij}\right)\left(\mathbf{y}, t-\frac{|\mathbf{x}-\mathbf{y}|}{c_0}\right) n_j \ \frac{dS}{|\mathbf{x}-\mathbf{y}|}
\end{aligned}
\tag{1}
$$

for the acoustic pressure p_a in the ambient medium, at the observer position $\mathbf{x}$ and the time t. p is the pressure, ρ the density, $\mathbf{u}$ the velocity field in the source domain V, S the surface of the solid boundaries and $\mathbf{n}$ the outward normal from the fluid, $T_{ij} = \rho u_i u_j + (p - c_0^2\rho)\delta_{ij} - \tau_{ij}$ is the Lighthill source term, where τ_{ij} are the viscous stresses and c_0 is the sound velocity in the ambient medium. The viscous contribution is negligible for flows with relatively high Reynolds numbers, and the approximated value of the Lighthill source term $T_{ij} \approx \rho u_i u_j$ is generally retained for isothermal flows at low Mach numbers. Note that the source quantities in the integrands of equation (1) have to be evaluated at retarded times $t - |\mathbf{x}-\mathbf{y}|/c_0$.

For a far field location at an observer point ($|\mathbf{x}| \gg |\mathbf{y}|$), [4] showed that (1) can be approximated by

$$
p_a(\mathbf{x},t) = \frac{1}{4\pi c_0^2}\frac{x_i x_j}{|\mathbf{x}|^3}\frac{\partial^2}{\partial t^2}\int\limits_V [T_{ij}]\, dV \tag{2}
$$

$$
- \frac{1}{4\pi}\frac{1}{|\mathbf{x}|}\frac{\partial}{\partial t}\int\limits_S [\rho u_i]\, n_i \ dS \tag{3}
$$

$$
- \frac{1}{4\pi c_0}\frac{x_i}{|\mathbf{x}|^2}\frac{\partial}{\partial t}\int\limits_S [\rho u_i u_j + p\delta_{ij}]\, n_j \ dS \tag{4}
$$

where [...] denotes the fact that the source quantities are evaluated at retarded times.

As stated by [4], the sound field can be viewed as the sum of three contributions: (i) the volume integral corresponding to (2) and representing the effects of the hydrodynamic fluctuations in the flow domain; (ii) the first surface integral corresponding to (3) representing the effect of mass flow rate fluctuations

through the surface and (iii) the second surface integral corresponding to (4) representing a flux of momentum and pressure through the surface. If there is zero normal velocity at the surface, only the surface integral associated with the pressure remains.

From the equation of the acoustic pressure, dimensional analysis can be carried out in order to evaluate the scaling of the acoustic intensity I with the acoustic Mach number of the flow Ma. For compact sources, it is shown in [19, 4, 3] that the volume integral contribution (2) induces a scaling of I as Ma^8, while the surface contributions associated with (3) and (4) induce scalings of I as Ma^4 and Ma^6 respectively. In the present configuration of grid-generated turbulence, we consider only a flow at low Mach number, so the contributions of the surface integrals (3) and (4) are expected to be dominant, according to the Mach scaling laws. We choose to use a control surface S surrounding the actual solid surface of the grid (because the latter is very complex to define accurately). In such case where a shifted control surface S is used, the contributions of momentum flux through the control surface in (4) have to be retained, but the surface integral (3) associated with the mass flow rate is zero because the flow is stationary upstream of the grid (this contribution is also zero because the acoustic sources are estimated via incompressible DNS data). Finally, the formulation that we have retained here to estimate the acoustic pressure is only based on the surface integral (4).

It is important to note at this point that the present methodology based on the estimation of surface integrals actually accounts for the sound generation by the turbulent flow itself. In fact the surface integrals are not the actual physical sources of sound, but represent the diffraction by the solid surface of the sound generated by the turbulent flow. It is well known that the diffraction process is the main contributor to the sound production, for a flow at low Mach number, as shown by [9] in the case of the sound radiated by a flow around a cylinder.

The present acoustic methodology was successfully tested on the sound radiated by a flow of constant velocity U over a circular cylinder of diameter D (see figure 5). For simplicity, a low Reynolds number was considered with $Re = UD/\nu = 150$ allowing us to perform a purely 2D calculation in a computational domain of $L_x \times L_y = 20D \times 12D$ using the mesh $n_x \times n_y = 361 \times 217$. For this simple model problem, accurate reference data DNS have been made available by [12] through a direct computation of sound approach. Using the incompressible acoustic sources from the present 2D DNS combined with the acoustic prediction tool, a good agreement with the reference data of [12] has been shown by [8]. In this work, we consider the sensitivity of the prediction with respect to the distance between the location of the control surface and the body surface. As the distance between the control surface and the body surface is quite small, a reliable acoustic prediction can be obtained by taking

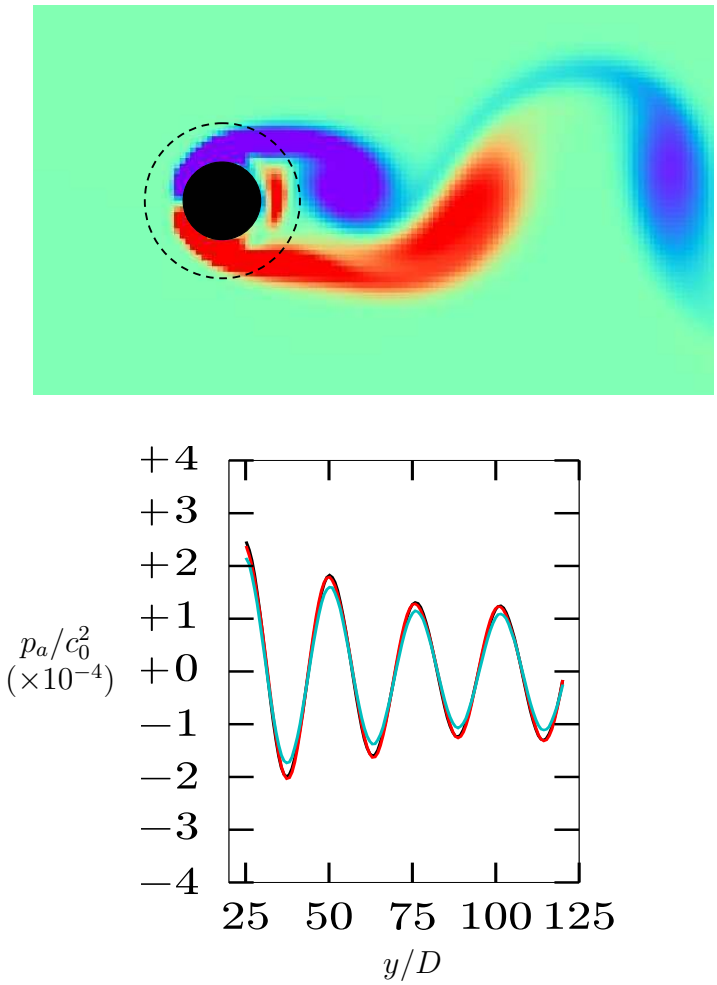

Fig. 5. *Acoustic prediction of the sound generated by the flow around a circular cylinder of diameter D, based on the surface integrals of equation 4. At the top, map of spanwise vorticity and surfaces used as control surfaces (cylinder in black and shifted surface with a diameter $2D$ in dashed line) ; at the bottom, acoustic pressure signals vs. distance of the cylinder centre obtained by using the solid surface as control surface in cyan, and that obtained by using the shifted surface as control surface in red.*

correctly into account the momentum flux contribution through the control surface as expressed in (4). For instance, it is clear from figure 5 that the acoustic pressure obtained by using a shifted control surface (the line in red in figure 5) compares very well with the acoustic pressure obtained by using the cylinder's solid surface as control surface (the line in cyan in figure 5).

The acoustic pressure in the present regular and fractal grid flow configurations is obtained from the surface data recorded at two planes S_1 / S_2, located at one mesh node before/after the grid and parallel to the grid, as shown in figure

6 . The final formulation of the acoustic pressure that we use in the present work can be expressed as

$$
\begin{aligned}
&-4\pi c_0\ p_a(\mathbf{x},t) = \\
&\frac{X}{R^2}\left\{\int_{S_1}\left[\frac{\partial p}{\partial t}\right]dS\ -\int_{S_2}\left[\frac{\partial p}{\partial t}\right]dS\right\} \\
&+\frac{X}{R^2}\left\{\int_{S_1}\left[\frac{\partial \rho u_x u_x}{\partial t}\right]dS\ -\int_{S_2}\left[\frac{\partial \rho u_x u_x}{\partial t}\right]dS\right\} \\
&+\frac{Y}{R^2}\left\{\int_{S_1}\left[\frac{\partial \rho u_x u_y}{\partial t}\right]dS\ -\int_{S_2}\left[\frac{\partial \rho u_x u_y}{\partial t}\right]dS\right\} \\
&+\frac{Z}{R^2}\left\{\int_{S_1}\left[\frac{\partial \rho u_x u_z}{\partial t}\right]dS\ -\int_{S_2}\left[\frac{\partial \rho u_x u_z}{\partial t}\right]dS\right\}
\end{aligned}
\tag{5}
$$

with (X, Y, Z) the coordinates of the observer point and $R = \sqrt{X^2 + Y^2 + Z^2}$. The computational estimations of the corresponding integrals have to be carried out carefully so as to take into account the difference in propagation distance between two source points because their respective contributions must be collected at different emission times so that they reach the observer point at the same time. It is therefore necessary to perform interpolations of the source fields known at discrete points and times to obtain the values at the exact position and time imposed by the integrals at retarded times. The results presented in the following section are obtained with the aid of an optimised acoustic algorithm which was developed to give access to acoustic fields generated by unsteady flows [20]. It is based on an advanced time approach [2] and an iterative selection of source-observer pairs involved in the sound generation process at a given time-step. It has already been used to compute successfully the sound radiated by a mixing layer [20] and a wake behind a cylinder [8].

4 Acoustic results

In this section, the procedure presented in the previous section is applied to the computation of the acoustic fields radiated by the flow and pressure fields from the DNS. From the simulation of each flow, 3200 source fields in the two surfaces S_1 and S_2 located at one mesh node before and after the grid (see figure 6) are stored during a time duration of 720 t_{min}/U_∞. Our acoustic predictions are made for a flow with a Mach number $Ma = U_\infty/c_0 = 0.1$. We start by computing the acoustic fields radiated in an observer plane located

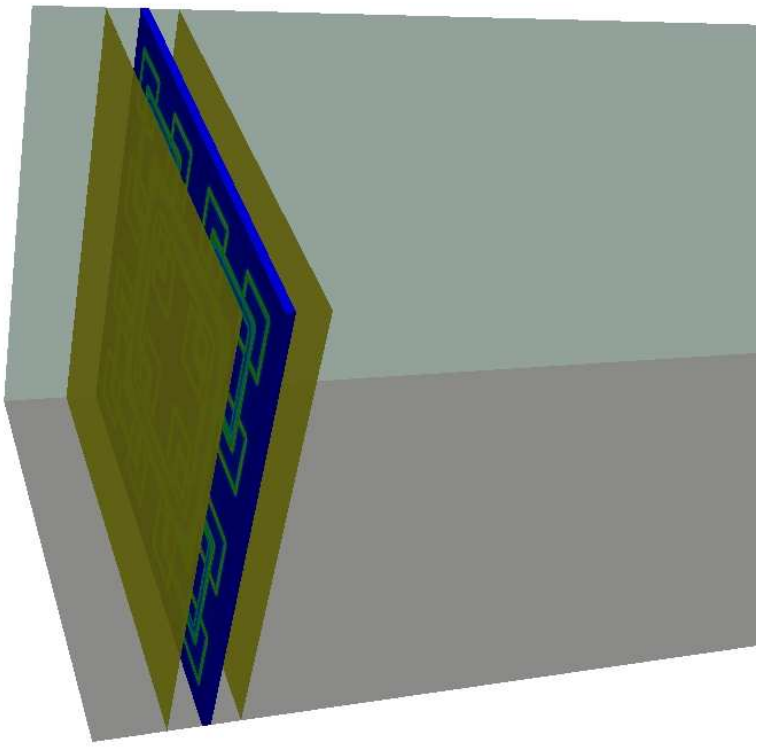

Fig. 6. *Schematic visualization of S_1 and S_2 inside the computational domain. S_1 is located one mesh before the fractal grid and S_2 is located one mesh after the fractal grid.*

at $Z = 0$. The observer plane of size 1000 $t_{min} \times 1000$ t_{min} contains 10^6 mesh nodes. Examples of these acoustic pressure fields at a given observer time are shown in figure 7 for both the regular and the fractal grids. There are clear differences between the two fields. Perhaps surprisingly, the fractal grid's acoustic field seems more regular than the regular grid's, and the number of wavefronts captured within the same area is lower in the case of the regular grid (about 4 wavefronts) than in the case of the fractal grid (about 10 wavefronts). The amplitudes of these wavefronts are also slightly larger for the fractal square grid than for the regular grid.

Figure 8 shows the time evolution of the acoustic pressure at a given observer location, the same location for both cases. As in figure 7 but even more clearly, we observe that the pressure signal corresponding to the fractal grid is more regular than for the regular grid, and that this regularity occurs at a relatively high frequency and with comparatively high amplitude. In these figures the contributions of the terms associated with the pressure and with the momentum flux are also shown. We note that the contribution associated with the momentum flux is dominant in the case of the flow generated by the fractal grid, while both contributions play a significant role in the case of the regular grid. Similar results are obtained for other observer locations.

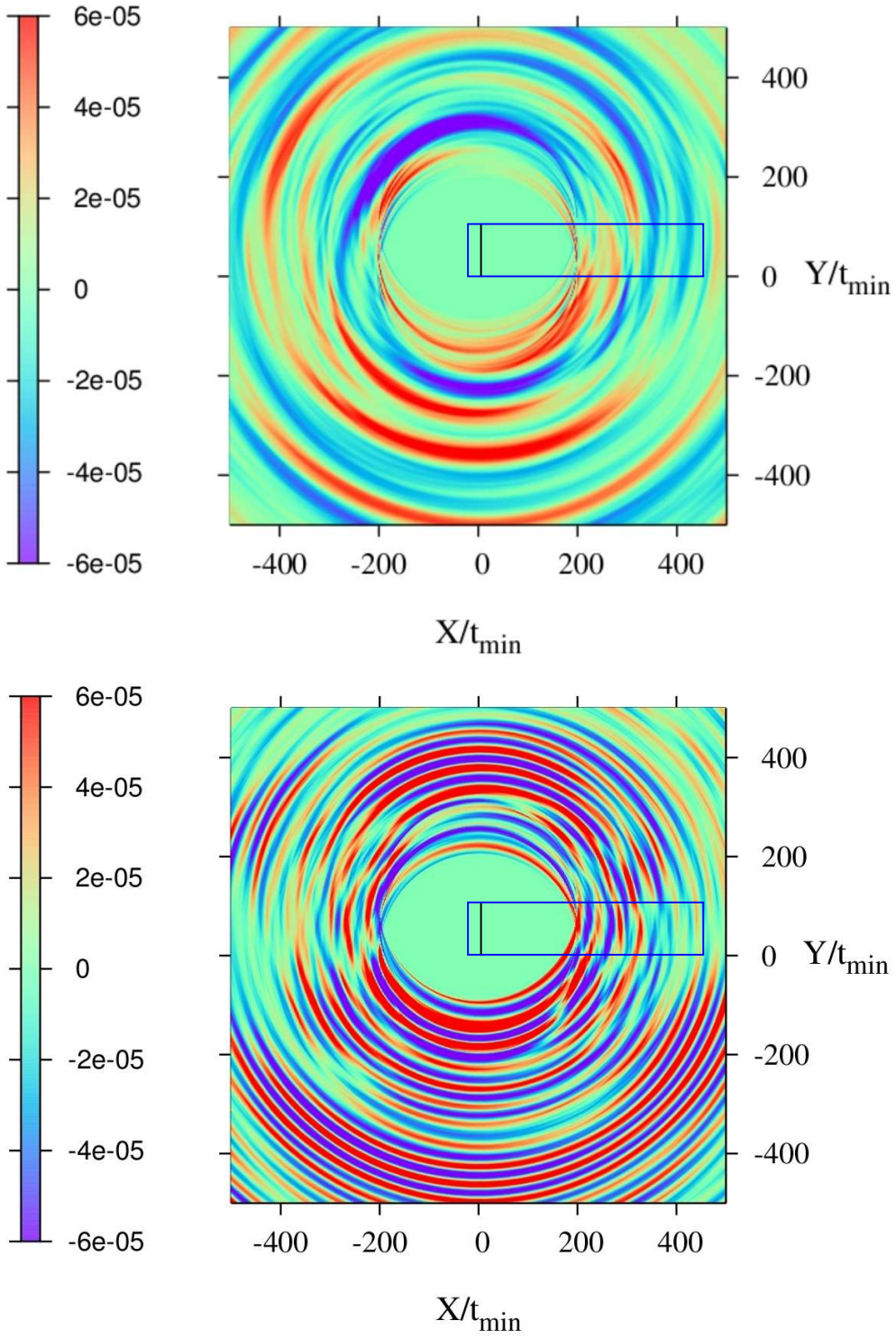

Fig. 7. *Acoustic pressure fields generated by the regular grid at top and by the fractal grid at bottom, in the observer plane* ($-500\ t_{min} < X < 500\ t_{min}$, $-500\ t_{min} < Y < 500\ t_{min}$, $Z = 0$), *at the observer time* $t = 81\ t_{min}/U_\infty$. *The centre of the regular/fractal grid is located at* $(0, 57.2t_{min}, 0)$. *The DNS computational domain is represented by a long rectangle on the center right of the pressure fields, and the grid is represented by a vertical line near the left size of the rectangle.*

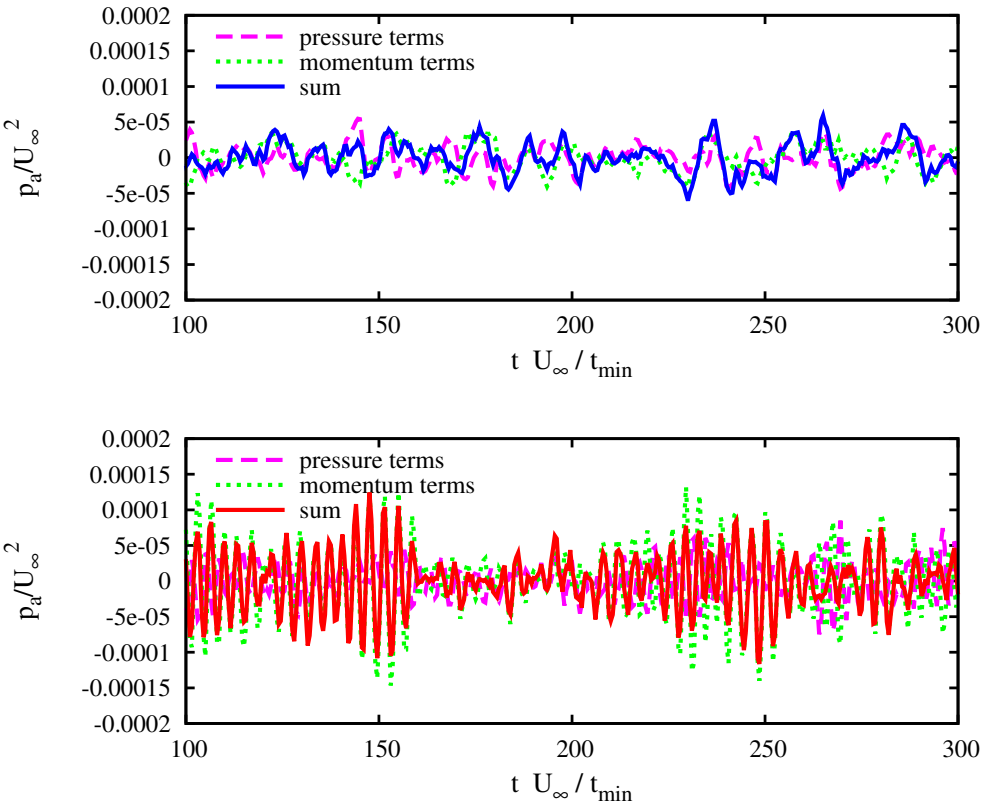

Fig. 8. *Sample of the time evolution of the acoustic pressure at the observer location* $(250\ t_{min}, 433\ t_{min}, 0)$*, corresponding to location 2 in figure 9, for the regular grid (top) and for the fractal grid (bottom).*

From our pressure signals at various observer locations we can obtain the frequency spectrum (in dB) corresponding to the Sound Pressure Level $SPL = 10log_{10}(p^2_{rms}/p^2_0)$ where p_{rms} is the root mean square of the pressure signal at a given location and $p_0 = 2{\times}10^{-5}Pa$ is the reference value in standard atmospheric conditions. For the computation of this spectrum the pressure signals are divided into seven overlapping sections windowed by a Hanning function. We plot the SPL spectrum as a function of dimensionless Strouhal number $St = ft_{min}/U_\infty$ where f is a frequency; see figure 9 where we plot the SPL spectrum SPL(St) at four different locations relative to the grid for both grids. The spectra corresponding to the fractal square grid and the regular grid are the red and blue curves respectively.

Our main finding is twofold. Firstly, the sound levels corresponding to the fractal grid are significantly reduced compared to those of the regular grid at Strouhal numbers smaller than 0.2. This is the range of frequencies where most of the sound lies in the case of the regular grid. Secondly, a well-defined peak appears at St between 0.2 and 0.3 in the case of the fractal grid. This peak is absent in the case of the regular grid and corresponds to the frequency of well-defined oscillations observed in figure 8 (bottom). This is a comparatively loud

peak reaching dB values higher than anything else in Figure 9. Note that the location and intensity of the peak are independent of the observer location. This peak observed in the sound levels can also be observed in the power spectra of the streamwise fluctuating velocity very close to the fractal square grid, as shown in figure 10 and previously observed in [17]. At a distance of $5M_{eff}$ downstream from the fractal square grid on the centreline of the flow, the power spectra of the turbulent kinetic energy exhibit a well-defined peak at a frequency similar to the peak observed in the sound levels. Further downstream from the grid, we observe a broad spectrum with an approximate $f^{-5/3}$ power-law shape for the fractal square grid but not for the regular grid.

Note that there is no peak in the frequency spectrum of the turbulent kinetic energy at a distance $5M_{eff}$ from the regular grid. This is a striking difference from what is observed with our fractal grid and can be explained as follows. Assuming that the peak at St between 0.2 and 0.3 originates from an approximately periodic street of vortices separated by a streamwise distance U_∞/f_s where f_s is the shedding frequency, then this vortex street can only exist if the distance from the grid where two neighboring wakes meet is much longer that about twice U_∞/f_s. As shown in [21] the distance from the grid where the wakes of two identical neighboring bars meet is approximately $0.5L_j^2/t_j$. The vortex street will therefore not have a chance to exist if $0.5L_j^2/t_j$ is smaller or comparable to $2U_\infty/f_s$. For a vortex street emanating from a bar of thickness t_j to be clearly present it is necessary that $2U_\infty/f_s \ll 0.5L_j^2/t_j$. Using $St_s \equiv \frac{f_s t_j}{U_\infty}$, this introduces a new dimensionless number $(L_j/t_j)^2 St_s$ and a related necessary condition for presence of an approximately periodic vortex street (assuming the Reynolds number allows it) which is $(L_j/t_j)^2 St_s \gg 4$. One usually expects St_s not to be too far from 0.2.

This criterion immediately explains why there is no peak in the frequency spectrum of the turbulent kinetic energy downstream of the regular grid where $(L_j/t_j)^2 = (M/t_b)^2 \approx 26.3$. When applied to the fractal grid, this criterion implies that only the wakes emanating from the smallest bars (of length $L_2 = L_y/8$ and thickness $t_2 = t_{min}$) can have a quasi-periodic vortex structure because $(L_2/t_2)^2 St_s \gg 4$. For the other size bars, $(L_1/t_1)^2 St_s$ and $(L_0/t_0)^2 St_s$ are larger though comparable to 4, hence no quasi-periodic vortex street structure can be expected from these larger bars. The peak in the frequency spectrum of the turbulent kinetic energy downstream of the regular grid must therefore be at a frequency f which corresponds to the shedding frequency of the smallest bars and is such that ft_{min}/U_∞ is around 0.2, as indeed we find.

The peak frequency in the energy spectrum corresponds to the peak frequency in the acoustic spectra, $St \equiv ft_{min}/U_\infty$ between 0.2 and 0.3. This peak in the acoustic spectrum is most probably the signature of the near-periodic vortex street emanating from the smallest bars on the fractal grid. The large number

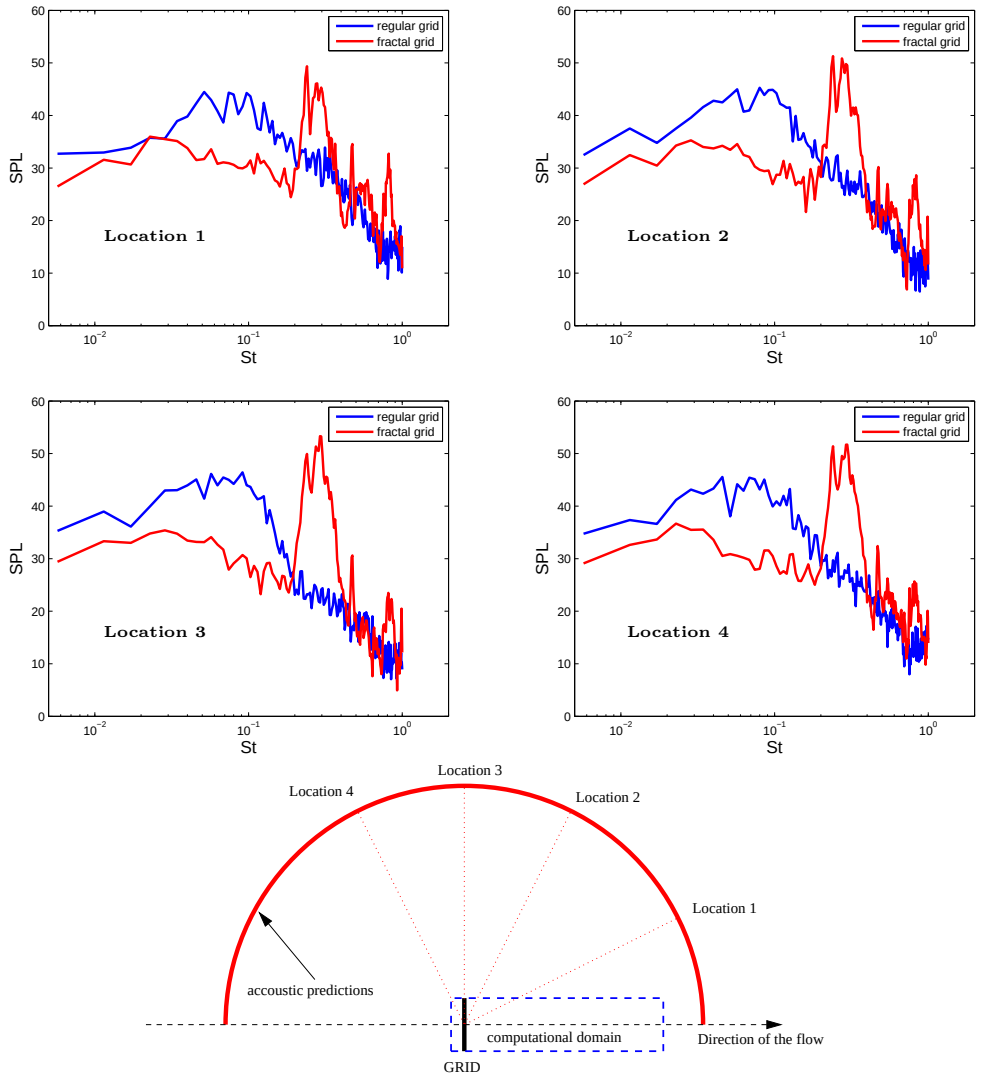

Fig. 9. *Comparison of acoustic spectra measured for four different locations for both grids.*

of smallest bars on our fractal grid (larger than the number of (L_0, t_0) and (L_1, t_1) bars) may explain the high intensity of the narrow-frequency sound they create. At frequencies higher than $St \approx 0.3$, the sound levels drop to relatively low values and two harmonics can be observed at Strouhal numbers approximately equal to 0.6 and 0.9. For an idea of the frequencies involved, a Strouhal number of 0.3 corresponds to $f = 5100Hz$ for $U_\infty = 0.1c_0$, $c_0 = 340m/s$ and $t_{min} = 2mm$ in which case this peak is barely audible to the human ear.

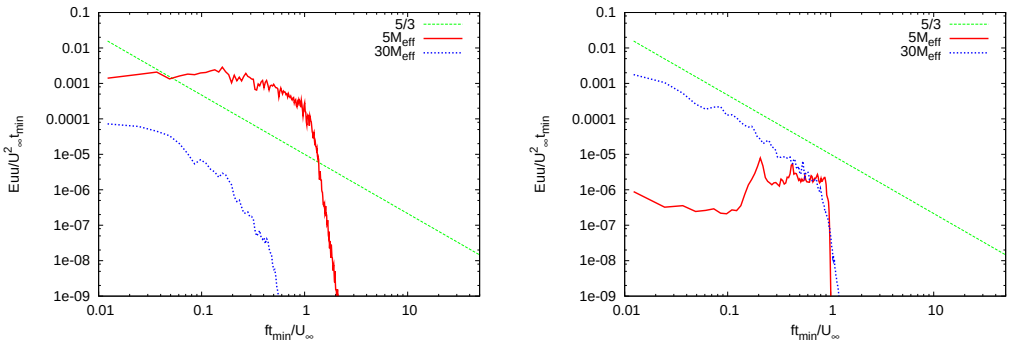

Fig. 10. *Power spectra of the streamwise velocity fluctuations in time for two different streamwise location on the centreline of the flow for the regular grid (left) and the fractal grid (right).*

5 Conclusion

In this work, we have shown that the sound levels corresponding to our particular fractal grid are significantly reduced compared to those of the regular grid at Strouhal numbers smaller than 0.2, and that a well-defined peak at St between 0.2 and 0.3 exists in the case of our particular fractal grid. We introduced a necessary condition for the existence of quasi-periodic vortex streets with well-defined peak acoustic frequencies which is that $(L_j/t_j)^2 St_s$ should be much larger than 4. Our regular grid does not satisfy this condition and therefore wakes from its different bars mix together too early for a clear periodic signal to be possible. On the other hand, our fractal grid is such that quasi-periodic fluid motions from the smallest bars are possible but not from the intermediate and larger ones. This new understanding of how peaks can appear in acoustic spectra originating from flows generated by fractal grids opens the possibility of designing fractal grids which are quieter than regular ones at the low frequencies without the presence of loud noise peaks at specific high frequencies. It also opens other possibilities, for example of creating a set of particular tunes.

A couple of important questions remain which will have to be addressed in future works.

(i) How does the fractal grid bring about the significant noise reduction at frequencies smaller than $St = 0.2$ compared to a regular grid of same porosity and same $Re_{M_{eff}}$?

(ii) The laboratory experiments of [22, 23] are different from the current numerical experiments in two main respects: the grids where designed as spoilers in the case of [22, 23] and had extra frames surrounding them; they were mounted on a wall thus making the boundary conditions different from our periodic ones. Nevertheless, both the laboratory and the numerical experi-

ments suggest a noise reduction in particular ranges of frequencies. When the fractal and the regular spoilers of [22, 23] were mounted at 90^o to the wall and to the incoming flow (as opposed to the 30^o inclination which these authors mostly studied) the fractal spoilers returned a noise reduction over all accessible frequencies (including between 300 Hz and $10000Hz$). Hence, boundary conditions as well as frames and different angles of attack can of course have very important influences on the acoustic signatures of fractal (and regular) grids and spoilers and will need to be addressed in detail in the future.

One of the difficulties, of course, is that the numerical studies required to address these questions rely on High Performance Computing and must therefore be limited in scope. Answers to the remaining open questions will require the design of different grids (some with more fractal iterations, i.e. larger N, some without perfect fractal iterative structure, i.e. R_L and R_t being different at different fractal iterations, some with different shapes of the main pattern of the grid which is square here but [11] also tried other patterns, etc); and they will also require DNS runs and Lighthill analogy calculations for a range of velocities, Reynolds numbers and Mach numbers.

Our results indicate that it is possible to passively shape the acoustic signatures of fractal aerodynamic objects such as spoilers, grids and fences just by adjusting their fractal design. Our results therefore warrant further research into this new topic.

Acknowledgements

The authors are grateful to Dr. Ning Li for helping with the parallel version of **Incompact3d** and David Froger for helping with the acoustic code. We also acknowledge support from EPSRC Research grants EP/E00847X/1 and EP/F051468/1 and we thank the DEISA Consortium (www.deisa.eu), co-funded through the EU FP6 project RI-031513 and the FP7 project RI-222919, for support within the DEISA Extreme Computing Initiative.

References

[1] C. Bogey and C. Bailly. Investigation of downstream and sideline subsonic jet noise using large eddy simulation. Theoret. Comput. Fluid Dynamics, 20(1):23–40, 2006.

[2] D. Casalino. An advanced time approach for acoustic analogy predictions. J. Sound Vib., 261:583–612, 2003.

[3] D.G. Crighton. Basic principles of aerodynamic noise generation. Progress in Aerospace Sciences, **16(1)**:31–96, 1975.

[4] N. Curle. The influence of solid boundaries upon aerodynamic sound. Proc. Roy. Soc. of London, series A, 231:505–513, 1955.

[5] J.E. Ffowcs-Williams and D. L. Hawkings. Sound generation by turbulence and surfaces in arbitrary motion. Proc. Roy. Soc. A, **264**:321–342, 1969.

[6] V. Fortuné, E. Lamballais, and Y. Gervais. Noise radiated by a non-isothermal, temporal mixing layer. part i: Direct computation and prediction using compressible dns. Theoret. Comput. Fluid Dynamics, 18:61–81, 2004.

[7] J. Freund. Noise sources in a low-Reynolds-number turbulent jet at mach 0.9. J. Fluid Mech., 438:277–305, 2001.

[8] D. Froger, V. Fortuné, and E. Lamballais. Acoustic analogy prediction using direct numerical simulation and immersed boundary method. In Ercoftac colloquium on IBM : current status and future research directions, Amsterdam, The Netherlands, 2009.

[9] X. Gloerfelt, F. Pérot, C. Bailly, and D. Juvé. Flow-induced cylinder noise formulated as a diffraction problem for low Mach number. J. Sound Vib., **287**:129–151, 2005.

[10] E. Groschel, W. Schröder, P. Renze, M. Meinke, and P. Comte. Noise prediction for a turbulent jet using different hybrid methods. Computers and Fluids, 37:416–426, 2008.

[11] D. Hurst and J. C. Vassilicos. Scalings and decay of fractal-generated turbulence. Phys. Fluids, **19**(035103), 2007.

[12] O. Inoue and N. Hatakeyama. Sound generation by a two-dimensional circular cylinder in a uniform flow. J. Fluid Mech., 471:285–314, 2002.

[13] S. Laizet and E. Lamballais. High-order compact schemes for incompressible flows: a simple and efficient method with the quasi-spectral accuracy. J. Comp. Phys., **228(16)**:5989–6015, 2009.

[14] S. Laizet, E. Lamballais, and J.C. Vassilicos. A numerical strategy to combine high-order schemes, complex geometry and parallel computing for high resolution dns of fractal generated turbulence. Computers and Fluids, **39(3)**:471–484, 2010.

[15] S. Laizet and N. Li. Incompact3d, a powerful tool to tackle turbulence problems with up to (10^5) computational cores. Int. J. Numer. Methods Fluids, **67(11)**:1735–1757, 2011.

[16] S. Laizet and J. C Vassilicos. Direct numerical simulation of fractal-generated turbulence. In Proc. DLES-7, Trieste, 2008.

[17] S. Laizet and J.C. Vassilicos. Dns of fractal-generated turbulence. Flow, Turbulence and Combustion, In Press, 2011.

[18] S. K. Lele. Compact finite difference schemes with spectral-like resolution. J. Comp. Phys., **103**:16–42, 1992.

[19] M. J. Lighthill. On sound generated aerodynamically I. General theory. Proc. Roy. Soc. A, 211:564–587, 1952.

[20] F. Margnat and V. Fortuné. An iterative algorithm for computing aeroacoustic integrals with application to the analysis of free shear flow noise.

J. Acoust. Soc. Am., **128(4)**:1656–1667, 2010.

[21] N. Mazellier and J.C. Vassilicos. Turbulence without Richardson-Kolmogorov cascade. Phys. Fluids, **22**(075101), 2010.

[22] J. Nedic, B. Ganapathisubramani, J.C. Vassilicos, J. Borée, L. Brizzi, and A. Spohn. Aero-acoustic performance of fractal spoilers. In 49th AIAA Aerospace Sciences Meeting Including The New Horizons Forum and Aerospace Exposition, Orlando, USA, 2011.

[23] J. Nedic, B. Ganapathisubramani, J.C. Vassilicos, J. Borée, L. Brizzi, and A. Spohn. Aero-acoustic performance of fractal spoilers. AIAA Journal, to appear, 2011.

[24] M. Terracol, E. Manoha, C. Herrero, E. Labourasse, S. Redonnet, and P. Sagaut. Hybrid methods for airframe noise numerical prediction. Theoret. Comput. Fluid Dynamics, 19(3):197–227, 2005.

[25] P. Valente and J.C. Vassilicos. The decay of turbulence generated by a class of multi-scale grids. J. Fluid Mech., In Press, 2011.